Available online at www.sciencedirect.com
SCIENCE DIRECT®
Nuclear Instruments and Methods in Physics Research A 547 (2005) 663–678
NUCLEAR INSTRUMENTS & METHODS IN PHYSICS RESEARCH Section A
www.elsevier.com/locate/nima

Determining axial fuel-rod power-density profiles from in-core neutron flux measurements

J. Kenneth Shultis*

Department of Mechanical and Nuclear Engineering, Kansas State University, 137B Ward Hall, Manhattan, KS 66506, USA

Received 27 October 2004; accepted 25 February 2005
Available online 10 May 2005

Abstract

A method is proposed for determining power-density profiles in nuclear reactor fuel rods from neutron flux measurements obtained by multiple in-core micropocket fission detectors (MPFD). A general formulation is presented that relates the power-density profiles in a reactor's fuel rods to the flux density at detector locations. Key to this formulation is the construction of an appropriate response function that relates the flux at any position in the core to the rate at which neutrons are born at different depths in the fuel rods. In this preliminary study simple, although not unrealistic, response functions for thermal neutrons and for fast neutrons are derived and used to illustrate the analysis methods.

To find the unknown power-density profiles in the fuel rods, given the measured fluxes at various locations through the core, requires inversion of an ill-posed Fredholm integral equation. With numerical quadrature, this integral equation can be converted into a (generally, underdetermined) set of algebraic equations for the power densities at various axial positions in the fuel rods. To solve these underdetermined equations, the linear regularization method is employed. Results are presented for simulated data for a single fuel rod and for multiple rods in various configurations. This preliminary study indicates that in-core flux measurements can indeed be used to infer power-density profiles in reactor fuel rods.
© 2005 Elsevier B.V. All rights reserved.

Keywords: Power-density profiles; Reactor power density; Inversion of in-core measurements; Deconvolution; Inverse problem

1. Introduction

If the distribution of fission neutron production is known throughout a thermal reactor core, various thermalization models can be used to predict the distribution of the resulting thermal neutrons. Likewise, various transport models can be used to estimate the neutron flux in any specified energy range. However, the inverse problem of using the thermal or fast flux distribution to infer the distribution of fission-neutron source strengths is not so straight forward. Certainly, if the thermal or fast flux is known at

*Tel.: +1 785 532 5626; fax: +1 785 532 6952.
E-mail address: jks@ksu.edu.

0168-9002/$ - see front matter © 2005 Elsevier B.V. All rights reserved.
doi:10.1016/j.nima.2005.02.046

only a single point in the core, then there is an infinity of fission source distributions that could produce this flux.

However, if the neutron flux could be measured in real-time at a great many positions throughout the core, then knowing the core geometry (i.e., the location, size and compositions of the fuel rods) it may be possible to make reasonable estimates of the fission profile in each fuel rod. Equivalently, the axial power-density distribution could be estimated for each fuel rod or assembly. This inverse problem of obtaining real-time power-density distributions from measured neutron fluxes is the subject of this paper.

2. Formulation of the inversion problem

To infer power-density profiles in fuel rods from in-core flux measurements it is first necessary to develop a mathematical model relating these quantities. In this section, we consider the general problem of a thermal-reactor core composed of K fuel rods, all of the same length $z_{\max}$. The rods are located in a homogeneous moderator material, and N small flux detectors are placed throughout the core in the moderator. The detectors are assumed to be point isotropic detectors of thermal or fast neutrons.

The power-density profile in the kth fuel rod, where z is the axial position measured from the top of the fuel rod, is denoted by $u^k(z)$ (W cm^{-3}). For simplicity, it is assumed that there are negligible self-shielding or radial flux depression in the rods, so that the power density varies only axially. For thermal fission of ^{235}U, the power density is proportional to the fast fission-neutron production rate density $S^k_{\rm fn}(z)$, i.e.,

$$S^k_{\rm fn}(z)\left(\frac{\text{fission neutrons}}{\text{cm}^3\,\text{s}}\right) = \kappa u^k(z)\left(\frac{\text{W}}{\text{cm}^3}\right) \tag{1}$$

where

$$\kappa = 2.43\left(\frac{\text{neutrons}}{\text{fission}}\right) \times (3.1\times 10^{10})\left(\frac{\text{fissions}\,\text{s}^{-1}}{\text{W}}\right) = 7.53\times 10^{10}\left(\frac{\text{neutrons}\,\text{s}^{-1}}{\text{W}}\right). \tag{2}$$

The fast fission neutrons quickly ($<10^{-3}$ s) slow and diffuse away from their point of birth. Let $\widehat{R}^k_i(z)$ be the flux density produced at position $\mathbf{r}_i$ in the moderator by a unit-strength disk source of fission neutrons with a radius equal to that of the fuel and at depth z in fuel rod k. The flux density at position $\mathbf{r}_i$ produced by fissions in fuel rod k is thus

$$\phi^k(\mathbf{r}_i) = \int_0^{z_{\max}} S^k_{\rm fn}(z)\widehat{R}^k_i(z)\,\mathrm{d}z. \tag{3}$$

The type of flux, e.g., thermal or fast, depends on the type of neutron detectors used for the in-core measurements, e.g., thermal or fast-neutron threshold detectors.

The response c_i (c for counts) of an point isotropic neutron detector at $\mathbf{r}_i$ is

$$c_i = D_i\sum_{k=1}^{K}\phi^k(\mathbf{r}_i) = D_i\sum_{k=1}^{K}\int_0^{z_{\max}} S^k_{\rm fn}(z)\widehat{R}^k_i(z)\,\mathrm{d}z, \quad i=1,\ldots,N \tag{4}$$

where D_i is the ith detector's response (counts, count rate, current, etc.) per unit neutron flux density. The expected detector measurement c_i can be expressed in terms of the power-density profiles of the fuel rods by using Eq. (1) to obtain

$$c_i = \sum_{k=1}^{K}\int_0^{z_{\max}} u^k(z)R^k_i(z)\,\mathrm{d}z, \quad i=1,\ldots,N \tag{5}$$

where the *detector response function* is defined as $R^k_i(z)\equiv\kappa D_i\widehat{R}^k_i(z)$.

Eq. (5) is a very general model relating the neutron detector measurements to the power-density profiles that are sought. The exact form of the detector response functions $R^k_i(z)$ depends on the energy of the neutrons detected and the geometry and composition of the core. In the next section models, albeit approximate, are given for $R^k_i(z)$ and which are subsequently used to demonstrate the feasibility of solving Eq. (5) for the power-density profiles $u^k(z)$.

3. Models for the detector response function

To use Eq. (5) to relate the power-density profiles to the measured data, it is first necessary

to determine the detector response function $R_i^k(z)$. In general, this is a very difficult problem requiring detailed transport calculations in a heterogeneous core geometry. The accurate determination of the response function is a crucial component of applying the methodology presented here to a particular reactor core. In this paper, which explores the feasibility of using in-core measurements to infer power-density profiles, two simple, although not unrealistic, detector response functions are introduced. One is for a thermal-neutron fission detector and is based on Fermi age and diffusion theory. The other is for a fission threshold detector and is based on the uncollided fast fission-neutron flux. For future studies, in which measured data are to be analyzed, more accurate transport-based response functions are presently being developed with the Monte Carlo MCNP code [1] for KSU's TRIGA reactor.

3.1. Thermalization kernel for a point fission source

To derive a simple model for $R_i^k(z)$, it is assumed the core can be treated as a quasi-homogeneous infinite medium and that Fermi-age and diffusion theories can be used to estimate the thermal flux arising from a point source of fission neutrons. From Fermi-age theory, a point isotropic source emitting $S_{\rm fn}$ fission neutrons per second produces a slowing down density $q_{\rm th}(r)$ of neutrons reaching thermal energies at distance r from the source [2]

$$q_{\rm th}(r) = \frac{S_{\rm fn}}{(4\pi\tau_{\rm T})^{3/2}} \exp[-r^2/(4\tau_{\rm T})] \tag{6}$$

where $\tau_{\rm T}$ is the age of fission neutrons to thermal energies. This slowing down density is then used as a thermal source term in the diffusion equation for the thermal flux density in spherical geometry. The general solution, given by Lamarsh [2] (with a corrected minus sign), is

$$\phi_{\rm th}(r) = \frac{L}{D}\left\{\frac{\sinh(r/L)}{r}\int_r^\infty r' \exp(-r'/L) q_{\rm th}(r')\,{\rm d}r' + \frac{\exp(-r/L)}{r}\int_0^r r' \sinh(r'/L) q_{\rm th}(r')\,{\rm d}r'\right\}. \tag{7}$$

Here L and D are the thermal diffusion length and diffusion coefficient, respectively, for the core material. Finally, substitution of Eq. (6) into this result and setting $S_{\rm fn} = 1$ one obtains the thermalization kernel

$$G_{\rm T}(r) = \frac{SL}{D(4\pi\tau_{\rm T})^{3/2}}\left\{\frac{\sinh(r/L)}{r}\int_r^\infty r' \times \exp(-r'/L)\exp[-r'^2/(4\tau_{\rm T})]\,{\rm d}r' + \frac{\exp(-r/L)}{r}\int_0^r r' \sinh(r'/L) \times \exp[-r'^2/(4\tau_{\rm T})]\,{\rm d}r'\right\}. \tag{8}$$

3.2. A thermal-neutron response function

Fission neutrons in most reactors core are produced in cylindrical fuel rods. In such reactors, it is proposed to place strings of small neutron detectors, each parallel to the fuel rods, throughout the core to obtain flux measurements at many core positions. To develop a thermalization model for a cylindrical fuel rod, consider a circular cross-section of a fuel rod of radius R as shown in Fig. 1. With respect to an origin at the center of this disk, a point isotropic detector is located at position $\mathbf{r} \equiv (x, y, z) = (d, 0, h)$. For this feasibility study, it is assumed that the diffusion properties of the fuel material and moderator are the same. For the TRIGA fuel rods to be used in the experimental phase of this study [3,4], there is roughly as much hydrogen in the ZrH fuel as in the water moderator. However, the thermal-neutron absorption cross-sections are quite different, and in later analysis studies the differences between fuel and moderator must taken into account. For the present, it is assumed that Eq. (8) is valid for this geometry. The thermal flux density at the detector from fission neutrons emitted isotropically from a differential area of the disk, $S_{\rm a}\,{\rm d}A = S_{\rm a}\rho\,{\rm d}\rho\,{\rm d}\theta$, is given by ${\rm d}\widehat{R}^{\rm th}_{\rm disk} = S_{\rm a} G_{\rm T}(r)\rho\,{\rm d}\rho\,{\rm d}\theta$, where $r = \sqrt{(d-\rho\cos\theta)^2 + \rho^2\sin^2\theta + d^2}$. Integration over the area of the disk (and using the angular symmetry of the problem) gives the thermal flux at the detector arising from fission neutrons

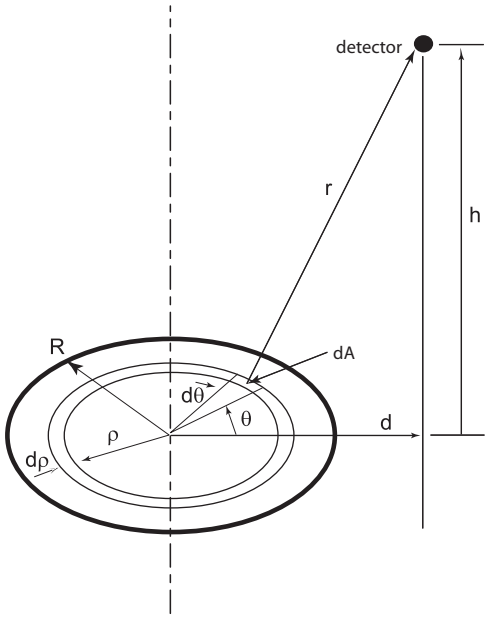

Fig. 1. Geometry for a disk fission-neutron source.

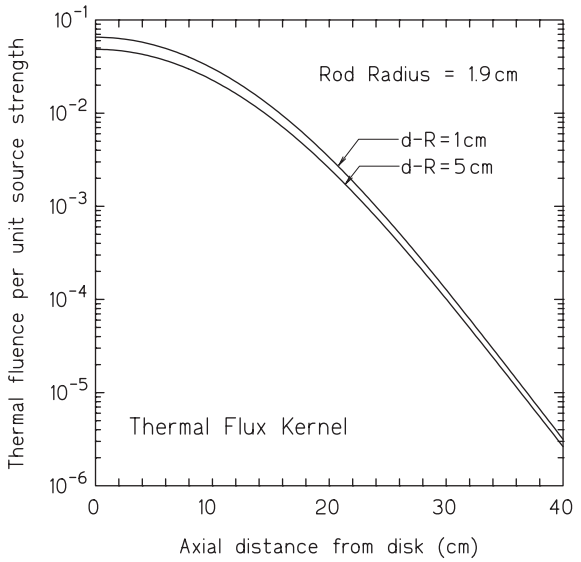

Fig. 2. The fuel-rod thermalization kernel $\widehat{R}^{\text{th}}_{\text{disk}}(R,d,r)$ of Eq. (9) for detectors in water at two distances d from the fuel-rod axis.

emitted by the fuel-rod disk (with $S_a = 1$), namely,

$$\widehat{R}^{\text{th}}_{\text{disk}}(R,d,z) = 2\int_0^R \rho\,\mathrm{d}\rho \int_0^\pi \mathrm{d}\theta G_{\text{T}}(r) \simeq 2\sum_{i=1}^{N_\rho} \rho_i \Delta\rho \times \sum_{j=1}^{N_\theta} \Delta\theta G_{\text{T}}(r(\rho_i,\theta_j,h,d)). \quad (9)$$

Here, equimeshes in the radial and angular directions are used to evaluate the double integral over the source disk using N_ρ and N_θ intervals, respectively. Finally, the detector response function is $R_i(z) = \kappa D_i \widehat{R}^{\text{th}}_{\text{disk}}(R,d,z)$. An example, of the fuel-rod thermalization kernel of Eq. (9) is shown in Fig. 2 for a water medium.

3.3. A fast-neutron response function

One type of micropocket fission detector (MPFD) being developed for in-core monitoring [3,4] is a fast-fission ^{232}Th gas detector that would respond to neutrons with energies only above about 2 MeV. The use of the fast flux to infer the axial power-density profiles is more attractive than use of the thermal flux, since the fast flux is far less affected by control material (e.g., control rods, soluble poisons, etc.) than is the thermal flux. Moreover, the fast flux above 1 MeV is very close to the uncollided flux of fission neutrons and, thus, more closely related to fissions in nearby regions of the fuel.

Consider the fuel rod cross-section disk shown in Fig. 3. The fission neutrons emitted isotropically from the differential area $\mathrm{d}A = \rho\,\mathrm{d}\rho\,\mathrm{d}\theta$ produce an uncollided flux $\mathrm{d}\phi_f^{\text{o}}$ at point a detector located at P_1, a radial distance d from the fuel rod axis and at an axial distance z from the disk, given by

$$\mathrm{d}\phi^{\text{o}}_{\text{fn}} = \frac{S_a\,\mathrm{d}A}{4\pi\ell^2}\exp[-\Sigma^{\text{F}}\ell^{\text{F}} - \Sigma^{\text{M}}\ell^{\text{M}}]. \quad (10)$$

Here S_a is the number of fission neutrons emitted per unit area of the fuel rod disk per unit time, ℓ the distance from $\mathrm{d}A$ to the detector, $\ell^{\text{F}}/\ell^{\text{M}}$ the distance neutrons travel in the fuel rod/moderator to reach the detector, and $\Sigma^{\text{F}}/\Sigma^{\text{M}}$ is the total macroscopic cross-section for the fuel/moderator, averaged over the fission neutron energy spectrum above the threshold energy of the fast neutron detector.

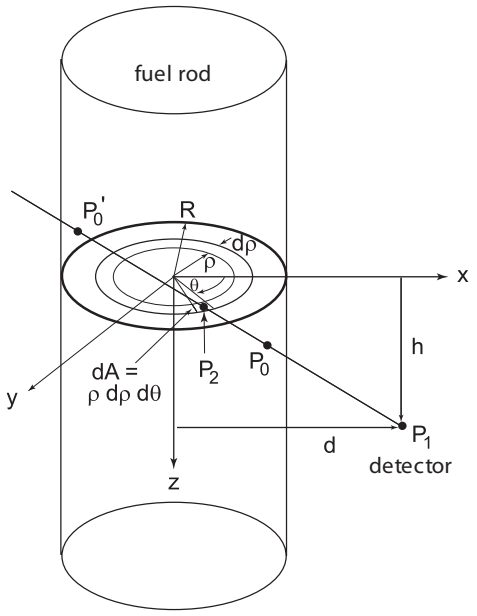

Fig. 3. Geometry for uncollided fast-flux kernel for a disk fission-neutron source.

To calculate the distances ℓ^{F} and ℓ^{M}, the coordinates of the point P_{o} where the line joining P_1 (the detector) and P_2 (the differential source area $\mathrm{d}A$) intersects the cylindrical fuel rod surface are needed. With respect to a Cartesian coordinate system centered on the disk center, the coordinates of points P_1 and P_2 are $(x_1 = d, y_1 = 0, z_1 = z)$ and $(x_2 = \rho\cos\theta, y_2 = \rho\sin\theta, z_2 = 0)$, respectively. The line through points P_1 and P_2 is given parametrically by

$$\begin{aligned} x &= x_1 + s(x_2 - x_1) \\ y &= y_1 + s(y_2 - y_1) \\ z &= z_1 + s(z_2 - z_1). \end{aligned} \tag{11}$$

The parameter s is the fraction of the distance ℓ between P_1 and P_2 at which the point (x, y, z) on the line lies from P_1. The equation of the cylindrical fuel rod surface is $x^2 + y^2 - R^2 = 0$, which upon substitution for x and y from Eq. (11), gives

$$[x_1 + (x_2 - x_1)s]^2 + [y_1 + (y_2 - y_1)s]^2 - R^2 = 0. \tag{12}$$

This is a quadratic equation for the parameter s whose two solutions s_- and s_+ correspond to the two intersection points P_0 and P_0' of the line with the cylinder. These values are (with $x_1 = d$ and $y_2 = 0$)

$$s_\pm = \frac{(x_2 - d)d}{(d - x_2)^2 + y_2^2} \times \left\{ 1 \pm \sqrt{1 - \frac{(d - x_2)^2 + y_2^2}{d^2 + (d - x_2)^2}(d^2 - R^2)} \right\}. \tag{13}$$

The smallest root $s_{\min} \equiv s_- < 1$ corresponds to the intersection point P_0 nearest the detector, while $s_{\max} \equiv s_+ > 1$ corresponds to the intersection point on the opposite side of the fuel rod surface. The distance from P_1 to P_0 ℓ is thus $\ell^{\mathrm{M}} = s_{\min}\ell$ and the distance from P_0 to P_2 is $\ell^{\mathrm{F}} = (1 - s_{\min})\ell$ where the distance from P_1 to P_2 is

$$\begin{aligned} \ell &= \sqrt{(x_1 - x_2)^2 + (y_1 - y_2)^2 + (z_1 - z_2)^2} \\ &= \sqrt{(d - \rho\cos\theta)^2 + \rho\sin\theta^2 + z^2}. \end{aligned} \tag{14}$$

The uncollided fast-flux kernel $\widehat{R}^{\mathrm{fn}}_{\mathrm{disk}}$ is then obtained (with $S_{\mathrm{a}} = 1$) by integrating Eq. (10) over all $\mathrm{d}A$ on the disk source, namely

$$\begin{aligned} \widehat{R}^{\mathrm{fn}}_{\mathrm{disk}}(R, d, h) &= \int_{\mathrm{o}}^{2\pi} \mathrm{d}\theta \int_0^R \mathrm{d}\rho\, \rho\, \mathrm{d}\phi^{\mathrm{o}}_{\mathrm{fn}}(\rho, \theta) \\ &= 2\int_{\mathrm{o}}^{\pi} \mathrm{d}\theta \int_0^R \mathrm{d}\rho\, \frac{\rho}{4\pi\ell^2} \\ &\quad \times \exp[-\Sigma^{\mathrm{F}}\ell^{\mathrm{F}} - \Sigma^{\mathrm{M}}\ell^{\mathrm{M}}] \\ &\simeq \frac{\Delta\rho\ \Delta\theta}{2\pi} \sum_{i=1}^{N_\rho} \sum_{j=1}^{N_\theta} \frac{\rho_i}{\ell_{ij}^2} \\ &\quad \times \exp[-\Sigma^{\mathrm{F}}\ell_{ij}^{\mathrm{F}} - \Sigma^{\mathrm{M}}\ell_{ij}^{\mathrm{M}}]. \end{aligned} \tag{15}$$

This last result is obtained by numerical quadrature in which the $(0, \pi)$ angular range and $(0, R)$ radial range are approximated by N_θ and N_ρ equimesh angular and radial intervals $\Delta\theta$ and $\Delta\rho$, respectively. Finally, the fast-neutron detector response function is $R_i(z) = \kappa D_i R^{\mathrm{fn}}_{\mathrm{disk}}(z)$.

For the TRIGA reactor, $\Sigma^{\mathrm{F}} \simeq 0.30\,\mathrm{cm}^{-1}$ and $\Sigma^{\mathrm{M}} \simeq 0.14\,\mathrm{cm}^{-1}$. The fast uncollided kernel of Eq. (15) is illustrated in Fig. 4 along with results obtained by MCNP [1] for the same infinitely long

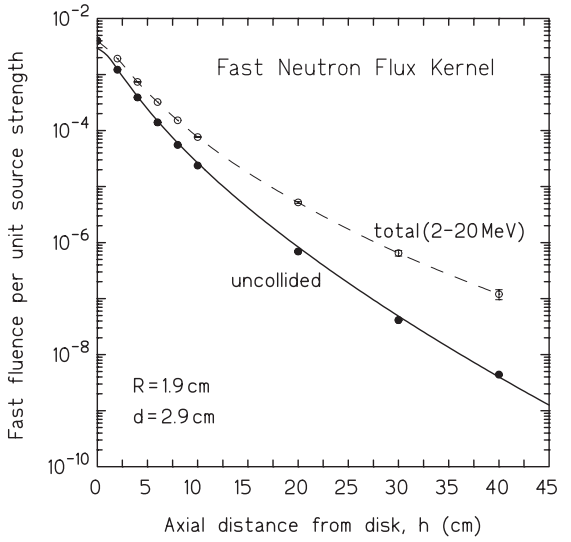

Fig. 4. The uncollided fast fission-neutron kernel $\widehat{R}^{\mathrm{fn}}_{\mathrm{disk}}(R,d,r)$ of Eq. (15) (solid line) for detectors 1 cm from the surface of an infinitely long TRIGA fuel rod. Also shown are MCNP results for the uncollided flux (solid circles) and the total flux (open circles and dashed line) for neutrons with energies between 2 and 20 MeV.

homogeneous fuel rod in an infinite water medium. For the MCNP calculations, a disk fission source was placed in the fuel rod and axially symmetric ring detectors were placed in the water around the fuel rod at various axial distances from the source. Both the uncollided and total flux of neutrons in the energy range 2–20 MeV were tallied. It is seen from Fig. 4 that the simple disk kernel of Eq. (15) with $\Sigma^{\mathrm{F}} = 0.30\,\mathrm{cm}^{-1}$ and $\Sigma^{\mathrm{M}} = 0.14\,\mathrm{cm}^{-1}$ givesremarkably good agreement with the MCNP results.

Of special note is the rapid fall-off with axial distance z of the detector from the disk source as compared to the thermal-neutron kernel shown in Fig. 2. This indicates that the fast flux should be much more sensitive to axial variations in the power-density profile in the fuel rod than would be the thermal flux. It also implies that fast neutron detectors respond primarily to neutrons born in immediately adjacent fuel rod region, whereas thermal flux detectors can be expected to be sensitive to neutrons born much farther away.

4. A nodal approximation for the inversion problem

To solve the Fredholm equations of Eq. (5) for the power-density profiles $u^k(z)$, these equations are first approximated by a set of linear algebraic equations for the power density $u^k_j \equiv u^k(z_j)$ at M specified depths z_j by using some appropriate numerical quadrature scheme to approximate the integrals. The resulting linear equations can be written as

$$c_i = \sum_{k=1}^{K} \sum_{j=1}^{M} R^k_{ij} u_j, \quad i = 1, \ldots, N \tag{16}$$

where R^k_{ij} is an $N \times M$ matrix.

This result can be simplified by combining all the unknown power densities u^k_j, $k = 1, \ldots, K$ into a single vector, namely

$$\mathbf{u} = \mathrm{col}[u^1_1, u^1_2, \ldots, u^1_M \times |u^2_1, u^2_2, \ldots, u^2_M| \ldots |u^K_1, u^K_2, \ldots, u^K_M]. \tag{17}$$

Then define the $N \times MK$ matrix

$$\mathbf{R} = (\,\mathbf{R}^1|\,\mathbf{R}^2|\quad \cdots |\,\mathbf{R}^K\,). \tag{18}$$

The N equations of Eq. (16) can thus be written compactly in vector notation as

$$\mathbf{c} = \mathbf{R}\mathbf{u}. \tag{19}$$

The reduction of Eqs. (5)–(16) can be effected by using numerical quadrature. A set of discrete depths z_j (usually equispaced) is selected with $z_1 = 0$ (the top of the fuel rods) and $z_M = z_{\max}$ (the bottom of the fuel rods). With this discrete spatial grid, Eq. (5) is decomposed into a sum of integrals over the subintervals as

$$c_i = \sum_{k=1}^{K} \int_0^{z_{\max}} \mathrm{d}z\, R^k_i(z) u^k(z) = \sum_{k=1}^{K} \sum_{j=1}^{M-1} \int_{z_j}^{z_{j+1}} \mathrm{d}z\, R^k_i(z) u^k(z). \tag{20}$$

The evaluation of the matrix elements R^k_{ij} in Eq. (16) depends on the specific quadrature scheme used. Results for three quadrature schemes are presented below.

4.1. An interval-average approximation

In this discretization, $u^k(z)$ in each of the subintervals in Eq. (20) is approximated by the average of its endpoint values. Thus Eq. (20) becomes

$$\begin{aligned} c_i &\simeq \sum_{k=1}^{K}\sum_{j=1}^{M-1}\frac{u_{j+1}^k+u_j^k}{2}\int_{z_j}^{z_{j+1}} R_i^k(z)\,\mathrm{d}z \\ &= \sum_{k=1}^{K}\sum_{j=1}^{M-1}\frac{1}{2}\left\{u_1^k\int_{z_1}^{z_2} R_i^k(z)\,\mathrm{d}z \right. \\ &\quad + \sum_{j=2}^{M-1} u_j^k\int_{z_{j-1}}^{z_{j+1}} R_i^k(z)\,\mathrm{d}z \\ &\quad \left. + u_M^k\int_{z_{M-1}}^{z_M} R_i^k(z)\,\mathrm{d}z\right\} \\ &= \sum_{k=1}^{K}\sum_{j=1}^{M} R_{ij}^k u_j^k \end{aligned} \tag{21}$$

where the elements of the $\mathbf{R}^k$ matrix are given by

$$R_{ij}^k = \frac{1}{2}\begin{cases} \int_{x_1}^{x_2} R_i^k(z)\,\mathrm{d}z, & j=1 \\ \int_{x_{j-1}}^{x_{j+1}} R_i^k(z)\,\mathrm{d}z, & j=2,\ldots,M-1 \\ \int_{x_{M-1}}^{x_M} R_i^k(z)\,\mathrm{d}z, & j=M. \end{cases} \tag{22}$$

4.2. A piecewise linear approximation

Here, it is assumed $u^k(z)$ varies linearly between its values at the endpoints of each subinterval, i.e.,

$$u^k(z) \simeq (z_{j+1}-z)u_j^k/\Delta_j + (z-z_j)u_{j+1}^k/\Delta_j, \quad z_j \leqslant z \leqslant z_{j+1} \tag{23}$$

where $\Delta_j \equiv (z_{j+1}-z_j)$. Substitution of this result into Eq. (20) gives

$$\begin{aligned} c_i = &\sum_{j=1}^{M-1}\frac{u_j}{\Delta_j}\int_{z_j}^{z_{j+1}}\mathrm{d}z\,(z_{j+1}-z)R_i^k(z) \\ &+ \sum_{j=1}^{M-1}\frac{u_{j+1}}{\Delta_j}\int_{z_j}^{z_{j+1}}\mathrm{d}z(z-z_j)R_i^k(z). \end{aligned} \tag{24}$$

This expression reduces to Eq. (16) in which the R_{ij}^k are given by

$$R_{ij}^k = \begin{cases} \int_{z_1}^{z_2}\mathrm{d}z f_1(z)R_i^k(z), & j=1 \\ \int_{z_{j-1}}^{z_{j+1}}\mathrm{d}z f_j(z)R_i^k(z), & j=2,\ldots,M-1 \\ \int_{z_{M-1}}^{z_M}\mathrm{d}z f_M(z)R_i^k(z), & j=M \end{cases} \tag{25}$$

with the weighting functions $f_j(z)$ defined as

$$f_j(z) = \begin{cases} (z-z_{j-1})/\Delta_{j-1}, & z_{j-1}\leqslant z<z_j \\ (z_{j+1}-z)/\Delta_j, & z_j \leqslant z<z_{j+1} \\ 0, & \text{otherwise.} \end{cases} \tag{26}$$

The integrals in Eq. (25), generally, must be evaluated using numerical integration.

4.3. A piece-wise quadratic approximation

Eq. (32) can also be approximated by

$$\begin{aligned} c_i &= \sum_{k=1}^{K}\int_0^{z_{\max}}\mathrm{d}z\,R_i^k(z)u^k(z) \\ &= \sum_{k=1}^{K}\sum_{j=1}^{M-2'}\int_{z_j}^{z_{j+2}}\mathrm{d}z\,R_i^k(z)u^k(z) \end{aligned} \tag{27}$$

where the prime on the summation indicates that the summation is over only odd values of j. For the approximation developed here, M is assumed odd. Now approximate $u^k(z)$ in each pair of adjacent subintervals by a quadratic function. For equally spaced nodes with $\Delta = z_{j+1}-z_j$, $u(z)$ in interval (z_j, z_{j+2}) is approximated by

$$\begin{aligned} u(z) \simeq &\frac{(z-z_{j+1})(z-z_{j+2})}{2\Delta^2}u_j^k - \frac{(z-z_j)(z-z_{j+2})}{\Delta^2}u_{j+1}^k \\ &+ \frac{(z-z_j)(z-z_{j+1})}{2\Delta^2}u_{j+2}^k. \end{aligned} \tag{28}$$

Substitution of this result into Eq. (27) gives Eqs. (16) where the R_{ij}^k are now

given by

$$R_{ij}^k = \frac{1}{2\Delta^2}\begin{cases} \int_{z_1}^{z_3} \mathrm{d}z\,(z-z_2) \\ \quad \times (z-z_3)R_i^k(z), \quad j=1 \\ \int_{z_{j-2}}^{z_j} \mathrm{d}z\,(z-z_{j-2}) \\ \quad \times (z-z_{j-1})R_i^k(z) \\ \quad + \int_{z_j}^{z_{j+2}} \mathrm{d}z\,(z-z_{j+1}) \\ \quad \times (z-z_{j+2})R_i^k(z), \quad j \text{ odd},\ j \neq 1, M \\ \quad -2\int_{z_{j-1}}^{z_{j+1}} \mathrm{d}z\,(z-z_{j-1}) \\ \quad \times (z-z_{j+1})R_i^k(z), \quad j \text{ even} \\ \int_{z_{M-2}}^{z_M} \mathrm{d}z\,(z-z_{M-2}) \\ \quad \times (z-z_{M-1})R_i^k(z), \quad j=M. \end{cases} \tag{29}$$

5. Estimating the power-density profiles

The inversion of Eq. (19) is an ill-posed problem since the number KM of unknowns (the u_j^k) is generally greater than the number N of measurements (the c_i). This means there are an infinite number of solutions because the solution space (of dimension KM) has a $(KM-N)$ dimensional degeneracy, i.e., any $(KM-N)$ components of $\mathbf{u}$ could be specified arbitrarily and still have Eq. (19) satisfied. To remove this degeneracy, the inversion problem must be *regularized* [5]. Such a regularized solution is obtained by solving the following minimization problem:

$$\text{minimize}: \quad \mathscr{A}[\mathbf{u}] + \lambda \mathscr{B}[\mathbf{u}] \tag{30}$$

where the positive functional $\mathscr{A}[\mathbf{u}]>0$ measures how well the vector $\mathbf{u}$ satisfies Eq. (19) and the positive functional $\mathscr{B}[\mathbf{u}]>0$ measures how well $\mathbf{u}$ satisfies whatever conditions are imposed to regularize the solution. Here λ is a parameter of the solution. As λ varies from 0 to ∞, the solution $\mathbf{u}(\lambda)$ varies along a *trade-off curve* between minimizing $\mathscr{A}$ (subject to constraint $\mathscr{B}=b$) and minimizing $\mathscr{B}$ (subject to constraint $\mathscr{A}=a$).

5.1. Linear regularization

Because the axial power profile in a fuel rod is generally a smoothly varying function of position z, linear regularization [5–9] is an obvious choice because, in this regularization method, smoothness constraints are imposed on the solution to remove the solution degeneracy. In this type of regularizaton, the functional $\mathscr{A}[\mathbf{u}]$ is chosen as the χ^2 statistic

$$\chi^2[\mathbf{u}] = \sum_{i=1}^{N}\sum_{j=1}^{KM}\left[c_i - \sum_{k=1}^{KM} R_{ik}u_k\right] \times S_{ij}^{-1}\left[c_j - \sum_{k=1}^{KM} R_{jk}u_k\right] \tag{31}$$

$$\approx \sum_{i=1}^{N}\frac{1}{\sigma_i^2}\left[c_i - \sum_{k=1}^{KM} R_{ik}u_k\right]^2 = |\mathbf{A}\mathbf{u}-\mathbf{b}|^2 \tag{32}$$

which measures how well $\mathbf{u}$ satisfies Eq. (19), with $\chi^2=0$ indicating an exact solution. Here $S_{ij} = \mathrm{Covar}[n_i, n_j]$ are the elements of the covariance matrix with n_i being the uncertainty or stochastic variation associated with the measured c_i. The approximate equality in the above result holds if one can neglect the off-diagonal covariance terms, with $\sigma_i^2 = \mathrm{Covar}[n_i, n_i]$. The matrix $\mathbf{A}$ has elements $A_{ij} = R_{ij}/\sigma_i$ and the vector $\mathbf{b}$ has elements $b_i = c_i/\sigma_i$.

The functional $\mathscr{B}[\mathbf{u}]$ is chosen as some measure of the smoothness of each of the $u^k(z)$ and is derived from first or higher derivatives of $u^k(z)$. In particular, the linear regularization method requires that $\mathscr{B}[\mathbf{u}] = \mathbf{u}^{\mathrm{T}}\mathbf{H}\mathbf{u}$ where $\mathbf{H}$ is some appropriate symmetric smoothing matrix. The inversion solution is thus determined by the following minimization problem:

$$\text{minimize}: \quad \mathscr{A}[\mathbf{u}] + \lambda\mathscr{B}[\mathbf{u}] = |\mathbf{A}\mathbf{u}-\mathbf{b}|^2 + \lambda\mathbf{u}^{\mathrm{T}}\mathbf{H}\mathbf{u}. \tag{33}$$

The matrix $\mathbf{H}$ is obtained by making some a priori assumption about the nature of the axial power-density profiles $u^k(z)$. Examples are given in Section 5.2.

To obtain the minimum of the functional of Eq. (33) and find $\mathbf{u}$, we write Eq. (33) in its

component form as

$$\mathscr{F}[\mathbf{u}] \equiv \mathscr{A}[\mathbf{u}] + \lambda\mathscr{B}[\mathbf{u}] = \sum_{i=1}^{N}\left[\sum_{j=1}^{KM} A_{ij}u_j - b_i\right]^2 + \lambda\sum_{i=1}^{KM} u_i \sum_{j=1}^{KM} H_{ij}u_j. \quad (34)$$

The values of u_j that minimize this functional are the solutions of the *KM normal equations* obtain by setting the derivative of $\mathscr{F}[\mathbf{u}]$ with respect to u_j to zero. Differentiation of Eq. (34) with respect to u_m, setting the result to zero, and use of the symmetry property of $\mathbf{H}$ gives

$$\sum_{j=1}^{KM}\left\{\left(\sum_{i=1}^{N} A_{im}A_{ij}\right) + \lambda H_{mj}\right\}u_j = \sum_{i=1}^{KM} A_{im}b_i, \quad m = 1,\ldots,KM \quad (35)$$

or, in matrix form,

$$(\mathbf{A}^{\mathrm{T}}\mathbf{A} + \lambda\mathbf{H})\mathbf{u} = \mathbf{A}^{\mathrm{T}}\mathbf{b}. \quad (36)$$

This set of KM linear algebraic equations is readily solved for $\mathbf{u}$ using standard techniques such as the Lower–Upper (LU) decomposition method or the singular-value decomposition (SVD) method [5].

Notice that before solving Eq. (36), one must first pick a value of λ. What value to pick? Ideally, λ should be as small as possible so as to force χ^2 to be as small as possible without loosing, through numerical roundoff, the effect of the smoothing component (the H-term) that forces a unique solution. As a starting point for the λ search, Press et al. [5] suggests

$$\lambda = \mathrm{Tr}(\mathbf{A}^{\mathrm{T}}\mathbf{A})/\mathrm{Tr}(\mathbf{H}) \quad (37)$$

where Tr is the matrix trace (sum of diagonal elements).

5.2. Smoothing matrices

In the linear regularization approach, the functional $\mathscr{B}[\mathbf{u}]$ is chosen as some measure of the collective smoothness of all the fuel rod profiles $u^k(z), k = 1,\ldots,K$. The functional $\mathscr{B}[\mathbf{u}]$ can be expressed as a sum of smoothness measures for each fuel-rod profile, namely

$$\mathscr{B}[\mathbf{u}] = \sum_{k=1}^{K}\mathscr{B}[\mathbf{u}^k] = \sum_{k=1}^{K}(\mathbf{u}^k)^{\mathrm{T}}\mathbf{H}^k\mathbf{u}^k = \mathbf{u}^{\mathrm{T}}\mathbf{H}\mathbf{u} \quad (38)$$

where the $\mathbf{u}$ vector one is seeking is that of Eq. (17) and the $KM \times MK$ block-diagonal matrix $\mathbf{H}$ is

$$\mathbf{H} = \begin{pmatrix} \mathbf{H}^1 & 0 & \cdots & 0 & 0 \\ 0 & \mathbf{H}^2 & \cdots & 0 & 0 \\ \vdots & & \ddots & & \vdots \\ 0 & 0 & \cdots & \mathbf{H}^{K-1} & 0 \\ 0 & 0 & \cdots & 0 & \mathbf{H}^K \end{pmatrix}. \quad (39)$$

The construction of the symmetric $M \times M$ submatrices $\mathbf{H}^k$ depends on the smoothness criterion chosen for the axial power-density profile for each fuel rod. In general, one can write

$$(\mathbf{u}^k)^{\mathrm{T}}\mathbf{H}^k\mathbf{u}^k = (\mathbf{u}^k)^{\mathrm{T}}[(\mathbf{B}^k)^{\mathrm{T}}\mathbf{B}^k]\mathbf{u}^k. \quad (40)$$

Several examples are given below.

5.2.1. Quadratic smoothing

If a quadratic function is a good approximation for $u^k(z)$ then, using forward finite difference, the following functional should be minimized:

$$\mathscr{B}[\mathbf{u}^k] \propto \int_0^{z_{\max}} [u^{k\prime\prime\prime}(z)]^2\,\mathrm{d}z \propto \sum_{j=1}^{M-3}[-u_j^k + 3u_{j+1}^k - 3u_{j+2}^k + u_{j+3}^k]^2. \quad (41)$$

$\mathbf{B}^k$ is the $(M-3)\times M$ matrix

$$\mathbf{B}^k = \begin{pmatrix} -1 & 3 & -3 & 1 & 0 & 0 & 0 & \ldots & 0 \\ 0 & -1 & 3 & -3 & 1 & 0 & 0 & \ldots & 0 \\ \vdots & & & & \ddots & & & & \vdots \\ 0 & \ldots & 0 & 0 & -1 & 3 & -3 & 1 & 0 \\ 0 & \ldots & 0 & 0 & 0 & -1 & 3 & -3 & 1 \end{pmatrix} \quad (42)$$

from which the $M \times M$ symmetric matrix $\mathbf{H}^k = (\mathbf{B}^k)^{\mathrm{T}}\mathbf{B}^k$ is obtained.

5.2.2. Second-order quadratic smoothing

The use of the first-order forward finite difference approximation for $u^{k\prime\prime\prime}(z)$ in Eq. (41) can be made more accurate for the nodes interior to the boundaries by using a second-order central

difference approximation, namely,

$$u_i^{k\prime\prime\prime} \propto [-u_{i-2}^k + 2u_{i-1}^k - 2u_{i+1}^k + u_{i+2}^k]/2, \qquad 2 < i < M-1. \tag{43}$$

With this approximation, and the first-order forward and backward finite difference approximation for $i = 1, 2, m-1$, and m, the $M \times M$ $\mathbf{B}^k$ matrix becomes

$$\mathbf{B}^k = \begin{pmatrix} -2 & 6 & -6 & 2 & 0 & 0 & 0 & \dots & 0 \\ 0 & -2 & 6 & -6 & 2 & 0 & 0 & \dots & 0 \\ -1 & 2 & 0 & -2 & 1 & 0 & 0 & \dots & 0 \\ 0 & -1 & 2 & 0 & -2 & 1 & 0 & \dots & 0 \\ \vdots & & & & \ddots & & & & \vdots \\ 0 & \dots & 0 & -1 & 2 & 0 & -2 & 1 & 0 \\ 0 & \dots & 0 & 0 & -1 & 2 & 0 & -2 & 1 \\ 0 & \dots & 0 & 0 & -2 & 6 & -6 & 2 & 0 \\ 0 & \dots & 0 & 0 & 0 & -2 & 6 & -6 & 2 \end{pmatrix}. \tag{44}$$

The resulting $\mathbf{H}^k = \mathbf{B}^{k\mathrm{T}}\mathbf{B}^k$ is an $M \times M$ symmetric matrix.

5.2.3. Cubic smoothing

Finally, we present the smoothing matrix for cubic smoothing. If one uses first-order forward finite differences for the fourth derivative, with cubic smoothing one tries to minimize

$$\mathscr{B}[\mathbf{u}^k] \propto \int_0^{z_{\max}} [u^{k\prime\prime\prime\prime}(z)]^2 \, \mathrm{d}z \propto \sum_{j=1}^{M-4} [-u_j^k + 4u_{j+1}^k - 6u_{j+2}^k + 4u_{j+3}^k - u_{j+4}^k]^2 \tag{45}$$

so that the $(M-4) \times M$ $\mathbf{B}^k$ matrix is

$$\mathbf{B}^k = \begin{pmatrix} -1 & 4 & -6 & 4 & -1 & 0 & 0 & \dots & 0 \\ 0 & -1 & 4 & -6 & 4 & -1 & 0 & \dots & 0 \\ \vdots & & & & \ddots & & & & \vdots \\ 0 & \dots & 0 & -1 & 4 & -6 & 4 & -1 & 0 \\ 0 & \dots & 0 & 0 & -1 & 4 & -6 & 4 & -1 \end{pmatrix} \tag{46}$$

from which the $M \times M$ symmetric matrix $\mathbf{H}^k = (\mathbf{B}^k)^{\mathrm{T}}\mathbf{B}^k$ is obtained. Finally, other higher-order polynomial smoothing schemes can be used [5,10] but those presented in this section are sufficient for the present study.

6. Example results

6.1. A single fuel rod

To determine the capabilities of the linear regularization (LR) method for the axial power-density problem, simulated data for point thermal-neutron detectors were constructed for specified power-density profiles. In this first example, a single fuel rod ($K = 1$) in an infinite moderator was considered. The rod considered had a radius $R = 1.9\,\mathrm{cm}$ and a length $z_{\max} = 38\,\mathrm{cm}$, typical of the fueled portion of a TRIGA fuel rod [11]. N equispaced thermal-flux detectors are placed in a line parallel to the rod axis and 1 cm from the rod surface. The first and last detectors are positioned opposite the ends of the fueled portion of the fuel rod.

Simulated detector responses c_i, for a given power-density profile were calculated from Eq. (5) with $K = 1$. With an adaptive Gaussian numerical integration and a specified power-density profile $u^1(z)$, values of the $\{c_i\}$ were calculated very accurately. These simulated ideal detector responses were then used to test the robustness of the LR method to estimate the power-density profile.

With the thermal-flux response function described in Section 3.2, simulated detector responses $\{c_i\}$ were generated for a typical power-density profile, which is frequently encountered in actual fuel rods, namely, a cosine-like distribution about the rods midpoint and depressed at the upper end by near-by control rods to give a "slumped" cosine shape. This profile is shown in Figs. 5 and 6 by the heavy dashed lines. With simulated c_i, the LR method was then used to reconstruct this profile.

The reconstructed power-density profile depends on the parameter λ that balances the trade-off between smoothness and accuracy of the profile as shown in Fig. 5. The smaller λ the better is the fit to the data, i.e., the smaller $\chi^2 \equiv \mathscr{A}[\mathbf{u}] \equiv |\mathbf{A}\mathbf{u} - \mathbf{b}|^2$ becomes. By contrast, as λ becomes large, the inverted profile becomes

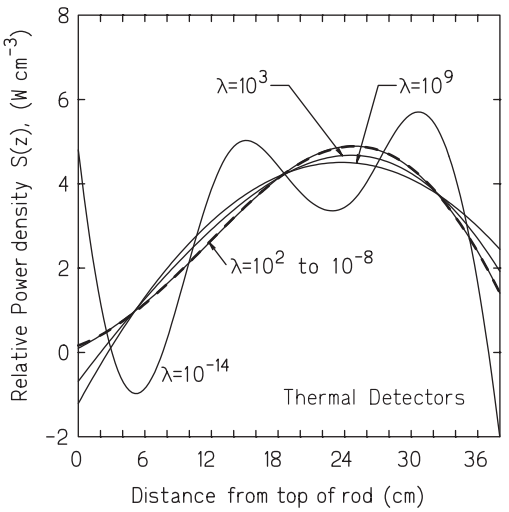

Fig. 5. LR estimated profiles using quadratic smoothing for several values of λ. The exact power-density profile is shown by the heavy dashed line. With 5 detector responses c_i, profiles were evaluated at $M = 51$ depths in the fuel rod and plotted with cubic spline interpolation.

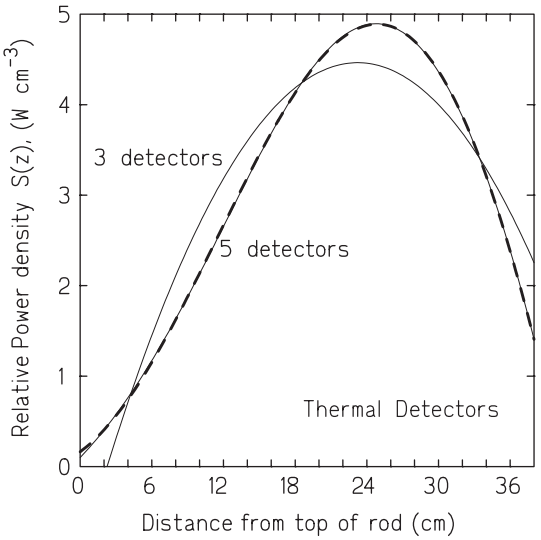

Fig. 6. The LR inverted power-density profiles ($M = 51$) using 3 and 5 detectors. The exact profile, with which the simulated detector response c_i were calculated, is shown by the heavy dashed line. Values of λ are those obtained from Eq. (37).

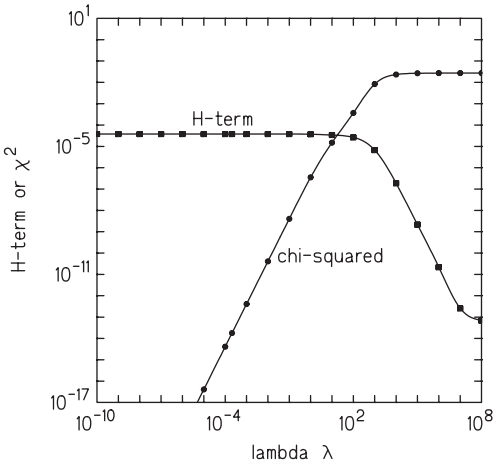

Fig. 7. Variation of the quadratic smoothness and accuracy components with λ for the problem shown in Fig. 5.

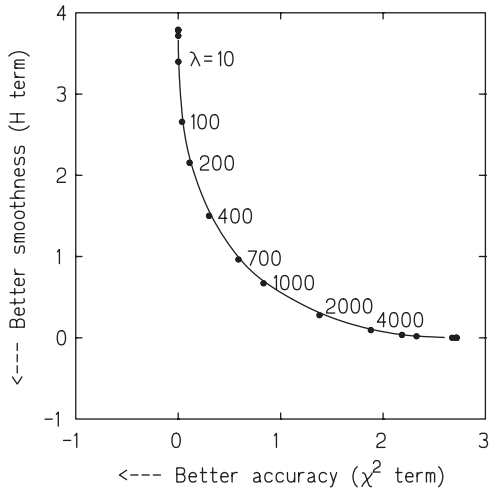

Fig. 8. The *trade-off curve* showing the variation with λ of the accuracy with the quadratic smoothness constraints shown in Fig. 5.

smoother and the fit becomes less accurate, i.e., $\mathbf{u}^T\mathbf{H}\mathbf{u}$ becomes smaller while χ^2 becomes larger. This behavior is illustrated in Figs. 7 and 8 which shows how χ^2 and $\mathbf{u}^T\mathbf{H}\mathbf{u}$ vary with λ. The *trade-off curve* shown in Fig. 8 dramatically illustrates show λ controls the compromise between accuracy and smoothness of the reconstructed profile. However, if too small a value of λ is used, the finite computer precision causes the regularization of the smoothing term to be lost and numerical instabilities arise (as seen in Fig. 5 for $\lambda = 10^{-14}$).

With the smooth specified power-density profile of Fig. 5 and the accurate evaluation of the c_i, information from relatively few detectors is needed to reconstruct the profile. In Fig. 6 it is seen that only 5 detectors are needed to reconstruct the profile (evaluated at $M = 51$ positions and plotted with cubic spline interpolation).

Because the simulated c_i values used in these examples are exact, i.e., they have no associated statistical uncertainties, the optimal (most accurate) computed profile is obtained with the smallest value of λ that can be used before numerical instabilities appear. These best-fit profiles, i.e., those with the smallest χ^2, represent the maximum capability of the inversion method since any real count data for the c_i have stochastic fluctuations, thereby degrading the inversion process.

In Fig. 7 it is seen that as λ increases beyond 10^2 the inverted profile assumes an increasingly quadratic shape, as prescribed by the quadratic smoothing constraint used, and the smoothing $\mathbf{u}^{\mathrm{T}}\mathbf{H}\mathbf{u}$ term decreases. With ideal simulated data, excellent reconstructed profiles are obtained for a wide range of λ. Fig. 7 shows the χ^2 component decreases continuously as λ decreases below $\lambda = 10^2$, indicating an increasingly more accurate profile. However, as seen from Fig. 5, essentially the same profile (2–3 significant figures) is obtained for $10^{-13} < \lambda < 10^2$. For this particular problem, the LR method is very robust in that the "best" reconstructed profile is very insensitive to the value of λ.

As seen in this example, the linear regularization method is capable of extracting quite reasonable profiles given only a small number of c_i values (here 5). When $u(z)$ is small near the top of the fuel rod, the computed profiles often yield small negative values. These spurious values are characteristic artifacts of the inversion process since linear regularization imposes no positivity constraint on the $u(z)$. One simplistic approach is simply to ignore such negative concentration estimates and to set the offending value to zero. However, such an ad hoc procedure is not very satisfying. The constrained LR (CLR) method [10] offers a more rigorous approach to eliminating such negative values in the reconstructed profile. This technique is to be investigated in future work.

7. Multiple fuel rods

For the case of K fuel rods, the power-density profiles at M equispaced axial depths are the components of the vector $\mathbf{u}$ of Eq. (17) where the superscript on the components refers to the fuel rod number and the subscript to the axial depth. With the linear regularization (LR) method described in Section 5.1, this vector of power densities is the solution of Eq. (36). For N detectors, the weighted response matrix $\mathbf{A}$ is the $N \times MK$ matrix

$$\mathbf{A} = (\,\mathbf{A}^1|\mathbf{A}^2|\quad \cdots|\mathbf{A}^K\,) \tag{47}$$

where the response matrix for the kth fuel rod $\mathbf{A}^k \equiv \mathbf{S}\mathbf{R}^k$ with $S_{ij} = (1/\sigma_i)\delta_{ij},\ i,j = 1,\ldots,N$. Here, σ_i is the standard deviation of the stochastic variation associated with the ith detector response c_i. For the case of "perfect" detector data (such as those generated for the simulations in this paper), $\mathbf{S} = \mathbf{I}$, the identity matrix. The $KM \times KM$ smoothing matrix $\mathbf{H}$ is given by Eq. (41), in which $\mathbf{H}^k$ is the $M \times M$ smoothing matrix for the kth fuel rod (see Section5.2). Finally, the weighted detector response vector $\mathbf{b} \equiv \mathbf{S}\mathbf{c} = \mathbf{c}$.

7.1. Computational considerations

There are several important considerations in using Eq. (36) to obtain the power-density profiles $\mathbf{u}$. First, the $MK \times MK$ matrix $\mathbf{D} \equiv \mathbf{A}^{\mathrm{T}}\mathbf{A} + \lambda\mathbf{H}$ must be evaluated. Even for a modest number of fuel rods ($K = 100$ say) and for fuel-rod profiles evaluated at say $M = 20$ axial locations, the $\mathbf{C}$ matrix begins to become sufficiently large (here 2000×2000) that evaluation of the $(MK)^2$ components can present a challenge to solve Eq. (36) sufficiently quickly to obtain power-density profiles in "real time."

If, during transient operation, the neutronic properties (cross-sections and geometry) do not change appreciably, $\mathbf{D}$ remains relatively constant and needs not be recomputed to invert another set of detector readings. For example, the responses of fast-neutron fission detectors are much less affected by control motion than are thermal-neutron fission detectors since the thermal

absorber in a control rod do little to shield an adjacent detector from fast neutrons.

Besides the time required to calculate the components of the **D** matrix, the memory required to store its components may be of concern when using a personal computer. For, example if $MK = 10,000$ then $10,000 \times 10,000$ double precision components requires 800 Mbytes of memory, memory that is available only in high-end personal computers. To avoid having to calculate and store the full **H** matrix of Eq. (39), its elements H_{ij} can be calculated as needed from the much smaller $M \times M$ submatrices $\mathbf{H}^k$ if the same smoothing regularization scheme is used for each fuel rod. In this case all the $\mathbf{H}^k$ are equal, and H_{ij} $i,j = 1,\ldots,MK$ can be computed readily from any one of the submatrices H^k_{ij} $i,j = 1,\ldots,M$, as follows. Let $k_i = (i-1)/M$ and $k_j = (j-1)/M$ where the "integer" division discards any fractional part. Then

$$H_{ij} = \begin{cases} 0, & k_i \neq k_j \\ H^k_{mn}, & k_i = k_j \end{cases} \tag{48}$$

where $m = i - (M \times k_i)$ and $n = j - (M \times k_j)$.

Another computational concern is how rapidly Eq. (36) can be solved for **u**. For modest sized problems with $MK < 200$, Eq. (36) can be solved directly using Gauss elimination or the LU decomposition technique [5] in a few seconds with present day personal computers. For much larger values of KM, matrix iterative techniques may be needed. In this study based on the KSU TRIGA reactor with only a sector of the core being investigated, the size of MK is such that the direct solution strategy using LU decomposition can be used.

7.2. Results for linear arrays

To test the linear regularization technique for multiple fuel rods, several simple linear arrays were analyzed. Arbitrary power-density profiles $u^k(z)$ were invented and simulated detector responses c_i were constructed by numerically evaluating Eq. (5). The detector response function $R^k_i(z)$ used was that of a fast-flux fission detector as described in Section 3.3. Again no stochastic uncertainty was introduced into the simulated data.

These simulated data were then unfolded or inverted using the linear regularization scheme. Results for two such analyzes are shown in Figs. 9 and 10. The actual power-density profiles are shown as continuous lines and the unfolded results at discrete axial locations are shown as solid circles. The agreement is remarkably good, indicating that, the linear regularization technique may be effective for analysis of real detector data.

In these simulation studies, the piecewise quadratic nodal approximation (see Section 4.3) was used to evaluate the elements R^k_{ij} of the response matrix using $M = 11$ equispaced axial depths for each fuel rod. The forward-difference quadratic smoothing matrix of Section 5.2.2 was used to regularize the inversion problems. Flux probes or strings, each with 5 equispaced, isotropic, fast-fission, point detectors, were positioned parallel to the fuel rods as shown by the smaller circles in the fuel rod arrays shown in Figs. 9–11. Thus, for the problem shown in Fig. 10 with $K = 8$ fuel rods and $N = 8 \times 5 = 40$ detectors, $MK = 88$ values of the power density are determined from the 40 detector responses.

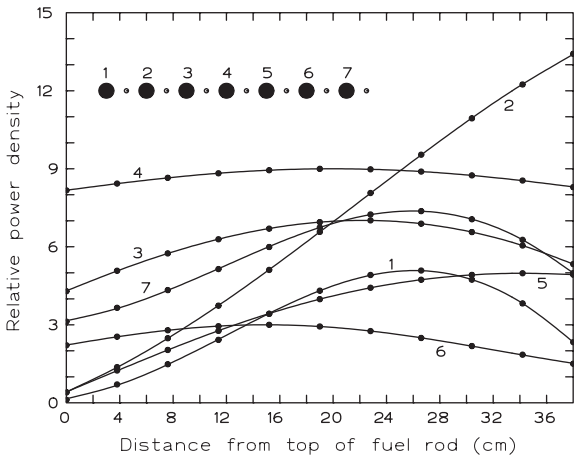

Fig. 9. Inverted power-density results ($M = 11$) from LR (solid circles) and the profiles (thin lines) used to generate the simulated detector data. The eight fuel rods (each 38 cm long and 3.8 cm in diameter) are in a linear arrays with a 2 cm water gap between adjacent rods. Detector strings (open circles) are midway between fuel rods with 5 fast-flux detectors per string.

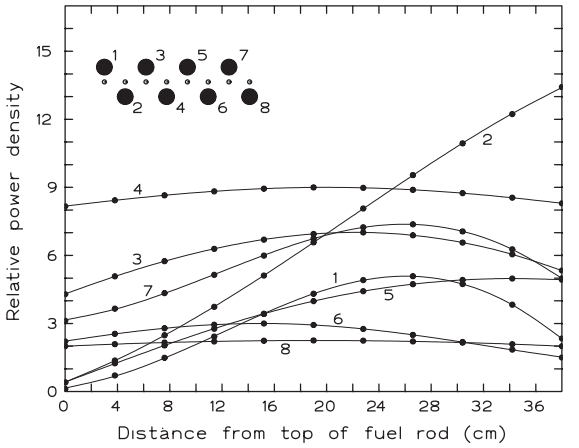

Fig. 10. Inverted power-density results ($M = 11$) from LR (solid circles) and the profiles (thin lines) used to generate the simulated detector data. The eight fuel rods (each 38 cm long and 3.8 cm in diameter) are placed in the shown triangular array with a 2 cm water gap between adjacent rods. Eight detector strings (open circles) are located at the centroids of the array with 5 fast-flux detectors per string.

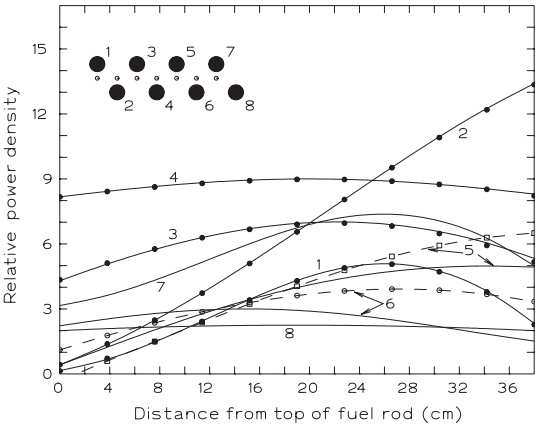

Fig. 11. Inverted power-density results ($M = 11$) from LR (solid circles) for the same case as Fig. 10 except the last detector string is absent. Good results are obtained for rods 1–4; however, inverted profiles for rod 5 (open squares) and rod 6 (open circles) deviated from the actual profiles. Results for rods 7 and 8 were meaningless.

From these and other examples, it was found that the number of detector strings needed to obtain good estimates of the power-density profiles had to equal or exceed the number of fuel rods. Moreover, the detector strings must be placed such that interchanging two fuel rods with different profiles would not give the same detector responses. An example of such a poorly configured array is shown in Fig. 11. This example is the same as that of Fig. 10 except the eighth detector string above rod 8 is omitted. Because the detectors respond primarily to fast neutrons born in the adjacent rods, the readings from the seventh string are little affected if rods 6 and 8 are interchanged. Thus, it is not surprising that the unfolded profiles begin to increasingly deviate from the actual profiles as the right-hand end of the array is reached. Unfolded profiles for rods 5 and 6 (open symbols) show significant errors, while the results for rods 7 and 8 were meaningless exhibiting very large negative and positive oscillations.

7.3. Simulated results for the KSU TRIGA reactor

It is planned to make flux measurements with new micropocket fission detectors (MPFD) in the core of KSU's TRIGA Mark II reactor [3,4]. To investigate the potential for inferring power-density profiles in the TRIGA fuel rods from such measurements, simulation studies were performed for the TRIGA lattice geometry [11]. The features of this core lattice are shown in Fig. 12. The sector of the core to be used for the experimental phase of this project is shown in Fig. 13.

To investigate the capabilities of the linear regularization technique to obtain power-density profiles for the TRIGA fuel rods, different power-density profiles $u^k(z)$ were created for each fuel rod shown in Fig. 13. Simulated detector responses c_i were then constructed by numerically evaluating Eq. (5). Again the short-range detector response function $R_i^k(z)$ of a fast-flux fission detector was used (see Section 3.3).

Example results are shown in Figs. 14–16. The unfolded power densities (11 values per fuel rod) are shown as symbols while the exact profiles used to generate the simulated data are the continuous lines. Again the unfolded results show remarkable agreement with the exact profiles. Only for the case of fuel rod 8 in Fig. 16 is disagreement apparent. Because of the short-range sensitivity of a fast-flux threshold fission detector, this disagreement is not surprising since fuel rod 8 is so far removed from

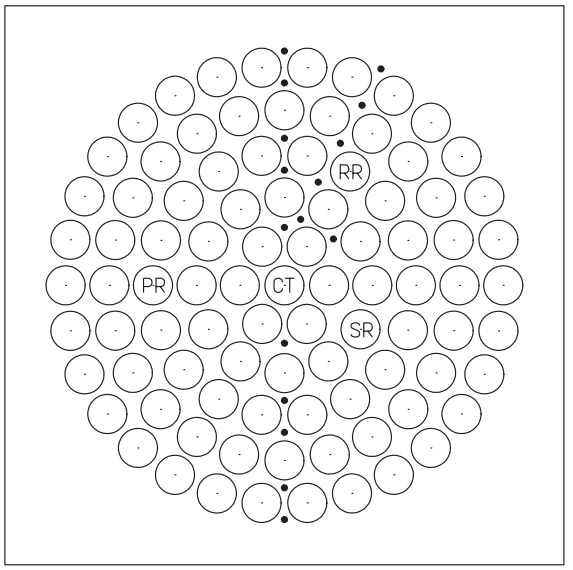

Fig. 12. A horizontal view of KSU's TRIGA core. Location of three control rods (SR, RR, and PR) and the water-filled central thimble (CT) are identified. Small solid circles are the available detector string locations [11].

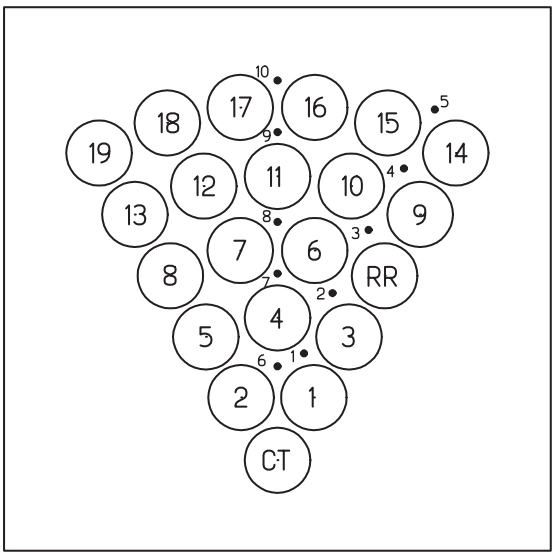

Fig. 13. The portion of the TRIGA core to be used for making flux measurements. Fuel rod numbers and flux probe hole numbers are shown. Fuel rods are 3.80 cm in diameter with a fuel length of 38 cm [11].

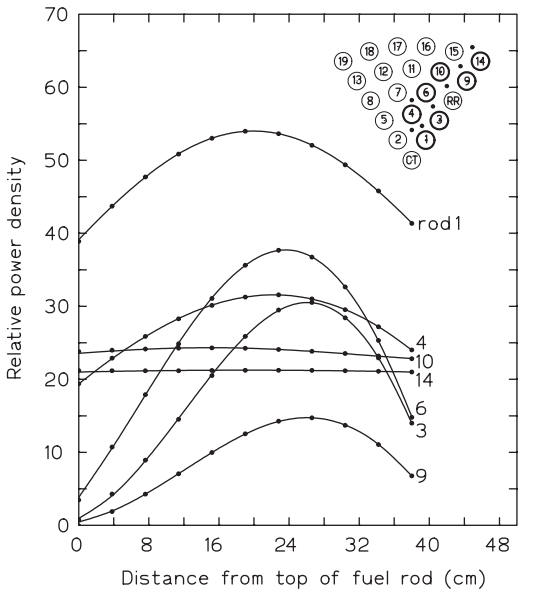

Fig. 14. Power-density profiles (lines) and unfolded results (solid circles) for seven fuel rods and seven fast-flux strings with 5 detectors each.

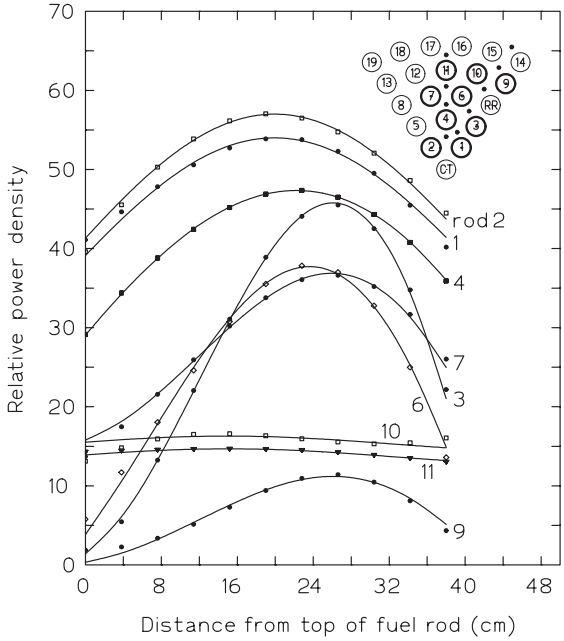

Fig. 15. Power-density profiles (lines) and unfolded results (solid circles) for nine fuel rods and nine fast-flux strings with 5 detectors each.

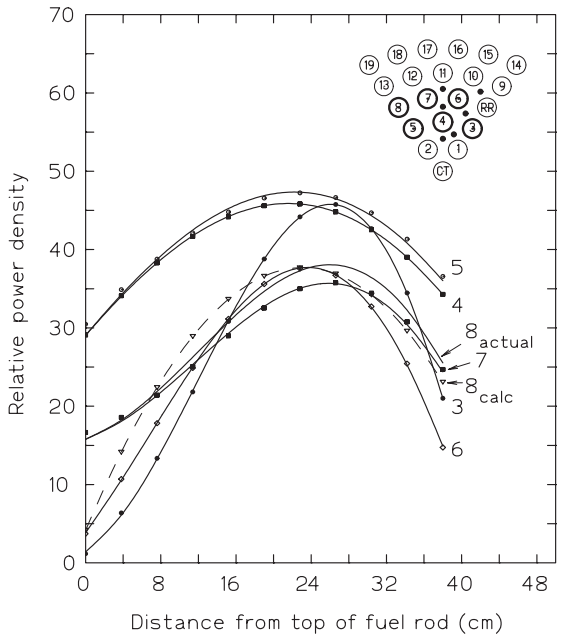

Fig. 16. Power-density profiles (lines) and unfolded results (solid circles) for six fuel rods six nine fast-flux strings with 5 detectors each.

the nearest detector string that neutrons born in this fuel rod have little influence on the detector responses.

Also, it should be noted that in this initial study of the TRIGA core, only the fuel rods whose power-density profiles were to be estimated were allowed to contribute to the simulated detector responses. The effect of having all fuel rods contribute to the simulated data is currently being investigated. However, since a fast-neutron detector's response is determined primarily by the adjacent fuel rods, unfolded profiles can be expected to be reasonably accurate provided all the adjacent fuel rods are included in the analysis.

8. Conclusions

From the results presented here, it is apparent that the linear regularization approach can be quite successful at inverting simulated in-core flux measurements. However, these results are based on idealistic detector response functions and "perfect" simulated data. To validate this methodology, realistic detector response functions must be obtained through detailed neutron transport calculations. Further the effect of noise in the detector system and the inherent stochastic variation in any radiation detection system must be investigated. Such investigations are ongoing, as well as the adaption of this methodology to the analysis of measurements from in-core micro-pocket fission chambers in KSU's TRIGA reactor.

Acknowledgements

This work was supported under the Department of Energy Research Initiative (NERI) Grant DE-FG07-02SF22611.

References

[1] MCNP, MCNP—A General Monte Carlo N-Particle Transport Code, vols. 1–3, LA-UR-03-1987, LA-CP-03-0245, LA-CP-03-0284, Los Alamos National Laboratory, 2003.
[2] J.R. Lamarsh, Introduction to Nuclear Reactor Theory, Addison-Wesley, Reading, MA, 1966.
[3] M.F. Ohmes, D.S. McGregor, J.K. Shultis, P.M. Whaley, A.S.M. Sabbir Ahmed, C.C. Bolinger, T.C. Pinsent, Proc. SPIE 5198 (2003) 234.
[4] D.S. McGregor, J.K. Shultis, M.F. Ohmes, A.S.M. Sabbir Ahmed, R. Ortiz, K. Hoffert, Micro-pocket fission detectors (MPFD) for near-core and in-core neutron flux monitoring, Presented at the ANS Fourth International Topical Meeting NPIC & HMIT, Columbus, OH, September 2004, 19.
[5] W.H. Press, S.A. Teukolsky, W.T. Vetterling, B.P. Flannery, Numerical Recipes, second ed., Cambridge University Press, Cambridge, 1992.
[6] A.N. Tikhonov, V.Y. Arsenin, Solutions of Ill-Posed Problems, Wiley, New York, 1977.
[7] S. Twomey, Introduction to the Mathematics of Inversion in Remote Sensing and Indirect Measurements, Elsevier, Amsterdam, 1977.
[8] I.J. Craig, J.C. Brown, Inverse Problems in Astronomy, Adam Hilger, Bristol, UK, 1986.
[9] J. Biemond, R.L. Lagendijk, R.M. Mersereau, Proc. IEEE 78 (1990) 856.
[10] J.K. Shultis, F. Khan, B. Letellier, R.E. Faw, Appl. Radiat. Isot. 54 (2001) 565.
[11] SAR, Safety analysis report, TRIGA Mark II nuclear reactor facility, Report Docket 50-188 to US Nuclear Regulatory Comm., Kansas State University, 11 September, 2002.